

Enhanced Drag of a Sphere Settling in a Stratified Fluid at Small Reynolds Numbers

KING YEUNG YICK¹, ROMAN STOCKER,¹
THOMAS PEACOCK¹ AND CARLOS R. TORRES²

¹Massachusetts Institute of Technology, Cambridge, MA 02139, USA

² Universidad Autonoma de Baja California, 22800 Ensenada, Mexico; and San Diego State University, San Diego, 92182 CA, USA

(Received ?? and in revised form ??)

We present a combined experimental and numerical investigation of a sphere settling in a linearly stratified fluid at small Reynolds numbers. Using time-lapse photography and numerical modelling, we observed and quantified an increase in drag due to stratification. For a salt stratification, the normalized added drag coefficient scales as $Ri^{0.51}$, where $Ri = a^3 N^2 / (\nu U)$ is the Richardson number, a is the particle radius, U its speed, ν the kinematic fluid viscosity, and N the buoyancy frequency. Microscale Synthetic Schlieren revealed that a settling sphere draws lighter fluid downwards, resulting in a density wake extending tens of particle radii. Analysis of the flow and density fields shows that the added drag results from the buoyancy of the fluid in a region of size $(\nu/N)^{1/2}$ surrounding the sphere, while the bulk of the wake does not influence drag. A scaling argument is provided to rationalize the observations. The enhanced drag can increase settling times in natural aquatic environments, affecting retention of particles at density interfaces and vertical fluxes of organic matter.

1. Introduction

The process of an object settling in a stratified fluid occurs ubiquitously in nature, with examples being the settling of marine snow aggregates through thermoclines and haloclines in oceans and lakes (MacIntyre *et al.* 1995), and dust in the atmosphere (Kellog 1990; Turco *et al.* 1990). Despite this ubiquity, the influence of stratification on settling has received little attention and remains poorly understood. Although conceptually simple, the problem is somewhat paradoxical: while stratification tends to suppress vertical fluid motion (Yih 1980), the settling process demands it.

The problem of particle motion in a homogeneous fluid is one of the oldest in fluid mechanics. The resistance to motion is described by a drag law, via a drag coefficient C_D that depends only on the particle's Reynolds number. For a sphere of radius a moving at speed U in a fluid of kinematic viscosity ν , the Reynolds number is $Re = Ua/\nu$ and a large body of experimental, theoretical and numerical work has established the dependence of C_D on Re (White 2005). The small Reynolds number regime, which is relevant to this paper, is reviewed by Leal (1980).

The presence of stratification significantly alters the problem of particle motion in a fluid. For a given stratification agent (e.g. salt or temperature) the dynamics depend on both Re and $Fr = U/(Na)$, where $N = [-(g/\rho_0)d\rho/dz]^{1/2}$ is the buoyancy frequency, ρ_0 a reference fluid density, g the acceleration of gravity, and $d\rho/dz$ the background density gradient. Furthermore, there is a distinct asymmetry between motion parallel and perpendicular to isopycnals (i.e. surfaces of constant density); since fluids are often vertically stratified, this corresponds to horizontal and vertical motion, respectively. Considerable attention has been devoted to horizontal motion, motivated by the design and opera-

tion of underwater vehicles and atmospheric flow past topography (Smith 1979, 1980; Greenslade 1994; Vosper *et al.* 1999). The tendency of stratification to suppress vertical motion (Yih 1980) drives flow primarily around, rather than over, a horizontally-moving three-dimensional body, while a two-dimensional body blocks a horizontal layer of fluid, the length of which scales linearly with the Richardson number $Ri = Re/Fr^2$ (Tritton 1988). For moderate to high Re ($\geq O(10^3)$), horizontal motion can generate internal waves, resulting in enhanced drag (Lofquist & Purtell 1984; Greenslade 2000; Scase & Dalziel 2004).

Considerably less work exists on vertically-moving bodies in stratified fluids. The simplest configuration, a two-layer fluid, was first investigated by Srdić-Mitrović *et al.* (1999), who measured the drag on a sphere settling through a thin density interface for $1.5 < Re < 15$. Their study revealed up to an order of magnitude increase in drag over the homogeneous case for $3 < Fr < 10$. The added drag resulted from the buoyancy of a tail of light fluid dragged down by the sphere. For the same configuration, Abaid *et al.* (2004) found a regime in which the sphere ‘levitates’, briefly reversing direction after crossing the interface. For a body smaller than the vertical extent of the stratification, consideration of a continuous stratification is more appropriate than a sharp interface; the simplest case being a linear stratification. Torres *et al.* (2000) numerically investigated the case of a sphere in the parameter regime $25 \leq Re \leq 100$ and $0.2 \leq Fr \leq 200$, finding C_D to strongly increase with Fr^{-1} for $Fr < 20$. The added drag was due to a rear buoyant jet, predicted by Eames *et al.* (2003) for an inviscid and non-diffusive fluid, associated with the return of isopycnals to their neutral density position. The existence of this jet, and the associated suppression of rear vortices, was supported by shadowgraph experiments at $Re \sim 800$ (Ochoa & Van Woert 1977). An increase of C_D with Fr^{-1} was

also observed by Higginson *et al.* (2003) for the related problem of a freely-rising horizontal grid of bars at $1000 \leq Re \leq 3000$ and $0.03 \leq Fr \leq 0.22$, and rationalized in terms of the buoyancy of displaced fluid in the wake of the grid. Although internal waves can exist for moderate to high Re (Warren 1960), in the aforementioned studies they were found not to contribute to drag. While a theoretical analysis (Zvirin & Chadwick 1974) suggests that stratification enhances drag even at $Re \ll 1$, predicting a dependence of C_D on $Ri^{1/3}$, there is a dearth of quantitative experimental data at small Reynolds numbers. Thus it still remains unclear whether settling particles experience added drag at $Re = O(1)$ and, if so, how this drag scales with stratification.

Here we present time-lapse photography, Microscale Synthetic Schlieren experiments and numerical simulations to quantify and rationalize the drag of small spheres settling in a salt-water stratification, and propose an empirical drag law for a linearly stratified fluid. The article is structured as follows. In section 2 we provide a formulation for the stratified drag coefficient and in section 3 we describe the experimental and numerical methods to measure it. Results are presented in section 4 and discussed in section 5, along with a scaling argument to support our findings.

2. Formulation of stratified drag coefficient

The drag force F_D on a sphere in a homogeneous fluid can be written as

$$F_D = -6\pi\mu aU - \frac{\rho V}{2} \frac{dU}{dt} - 6a^2\rho\sqrt{\pi\nu} \int_{-\infty}^t \left(\frac{dU}{dt} \right)_{t=s} \frac{ds}{\sqrt{t-s}}, \quad (2.1)$$

where V is the volume of the sphere, ρ the density of the fluid and μ its dynamic viscosity. The first term on the right is the Stokes drag for steady settling at speed U , the second is the added mass drag, arising because an accelerating sphere spends energy

in accelerating the surrounding fluid, and the third is the Basset history drag, due to diffusion of vorticity from an accelerating sphere as the boundary layer forms. The latter two terms are negligible under steady conditions. To adopt a consistent formulation of F_D across all Re , it is customary to write $F_D = C_D^H \frac{1}{2} \rho U^2 \pi a^2$, where the homogeneous drag coefficient C_D^H is a function of Re . For $Re \ll 1$, $C_D^H = 12/Re$. While the latter relation is somewhat misleading, since F_D is independent of Re in this regime, empirical extensions of this formulation prove useful to bridge the small and moderate Re regimes. A widely used empirical relation is

$$C_D^H = \frac{12}{Re} + \frac{6}{1 + \sqrt{2Re}} + 0.4, \quad (2.2)$$

which holds for $0 < Re < 2 \times 10^5$ with less than 10% error (White 2005).

The problem of a sphere settling in a linearly stratified fluid is illustrated in figure 1(a). Adopting the formalism for a homogeneous fluid, under quasi-steady conditions (defined below) we write the drag force in a stratified fluid as $F_D = C_D^S \frac{1}{2} \rho U^2 \pi a^2$, where the unknown stratified drag coefficient C_D^S captures the influence of stratification. For a given stratifying agent, we expect C_D^S to depend on Re and Fr . In general, C_D^S will also depend on the Prandtl number $Pr = \nu/D$, where D is the diffusivity of the stratifying agent. Here we focus on salt stratifications ($Pr = 700$) and briefly address temperature stratifications ($Pr = 7$).

Settling in a stratified fluid is an inherently unsteady process, because the density contrast between particle and surrounding fluid, hence the particle speed, decreases during settling: eventually the particle comes to rest at its depth of neutral buoyancy. We will see, however, that settling is quasi-steady for the parameter regime explored here, as added mass and Basset terms are negligible. Then, U is set by the balance of drag and

buoyancy forces:

$$C_D^S \frac{1}{2} \rho U^2 \pi a^2 = \frac{4}{3} \pi a^3 \Delta \rho g, \quad (2.3)$$

where $\Delta \rho = \rho_P - \rho$ is the density contrast and ρ_P the particle density. This yields

$$C_D^S = \frac{8ga}{3U^2} \frac{\Delta \rho}{\rho}, \quad (2.4)$$

which enables C_D^S to be determined from measurements of $\rho(z)$ and $U(z)$. To highlight the effect of stratification, one can normalize C_D^S by the locally homogeneous drag coefficient C_D^H from equation (2.2), here representing the drag coefficient the sphere would have if the entire water column had the density and viscosity of the fluid at that depth. The normalized drag coefficient

$$C_D^N = \frac{C_D^S}{C_D^H} \quad (2.5)$$

reveals whether stratification does ($C_D^N \neq 1$) or does not ($C_D^N = 1$) affect drag.

3. Methods

3.1. Drag measurement by time-lapse photography

Experiments were performed in a 30 cm high, 51 cm long and 26 cm wide plexiglas tank, with 0.54 cm thick walls. The tank was covered with a lid to eliminate convection in the fluid due to evaporation. An initial set of experiments was performed in homogeneous salt-water solutions of densities 1000, 1019 and 1035 kg m⁻³, measured with an Anton-Parr DMA38 densitometer. For all other experiments, the tank was filled with linearly stratified salt water using a double-bucket system (Oster 1965), and left to stand for at least five hours to dissipate any residual flows. To achieve larger density gradients, in some experiments the tank was first partially filled with fresh water, followed by linearly strat-

ified salt water up to a density ρ_S , and finally with homogeneous salt water of density ρ_S .

Spherical density floats (American Density Floats) with densities ranging from 1010.0 to 1130.0 kg m^{-3} in intervals of 10.0 kg m^{-3} were released into the tank to measure $d\rho/dz$. Regular vertical spacing of the floats confirmed the linearity of the density profile $\rho(z)$. The density gradient was determined from a linear fit to $\rho(z)$ and used to compute N , taking $\rho_0 = 1000 \text{ kg m}^{-3}$. The small size of the floats (diameter = 7 mm) and their location far from the settling path ($> 20 \text{ cm}$) ensured they did not affect the density field. There was no discernible motion of the floats, demonstrating the absence of any convection in the tank.

Polystyrene spheres of radius $a = 196$ and $390 \text{ }\mu\text{m}$ (Duke Scientific; coefficient of variation for a : 3%) and density $\rho_P = 1050 \text{ kg m}^{-3}$ were used in the experiments. To ensure the accuracy of ρ_P , we confirmed that the polystyrene spheres and the 1050 kg m^{-3} density float came to rest at the same depth. We measured the temperature of the fluid at the depth of each observation by a needle thermometer located far from the settling path. The temperature and the corresponding density were used to calculate the local dynamic viscosity μ (Fofonoff & Millard 1983), including the effect of salinity on viscosity. Before release, particles were mixed with a small amount of fluid from the surface of the tank and a minimal amount of soap as a wetting agent to prevent sticking. To ensure settling through the observation window, a single particle was released using a 1 ml pipettor through a partially submerged conical injector (a 1 ml pipette with its tip cut off) inserted in a 7 mm wide hole in the lid.

To avoid wall effects, the settling path was more than 5 cm ($> 125a$) from the nearest

wall of the tank, which corresponds to a less than 1% change in drag coefficient for a homogeneous fluid (Clift *et al.* 1978). The spheres settled in front of a black background and were illuminated by a fiber-optic light source. A ruler placed to the side of the settling path, and at the same distance from the camera, was used to calibrate vertical distances, and set vertical by use of a plumb line. Images were captured over a 3 cm tall observation window at 3 to 12 frames/s using a JAI CV-M4+CL CCD camera controlled by Digiflow (2006) and spheres were subsequently tracked with Matlab (The Mathworks, Natick, MA). A particle appeared as a light spot on a dark background, and the centre of the spot was taken as the position of the particle. The time series of vertical position was smoothed by a three-point moving average, before computing the particle velocity $U(z)$ using a four-point centre-difference approach (Dalziel 1992).

For each experiment, characterized by a given combination of N , a and $\Delta\rho$, ten replicate runs were performed to reduce errors associated with such factors as variability in particle size and injection conditions. At each vertical location, the mean velocity was computed as the average over these ten runs, as shown in figure 2(a). The mean velocity profile, in combination with $\rho(z)$, determined Re , Fr , $Ri = Re/Fr^2$, and C_D^N , which all varied over the vertical length of the observation window since $\rho(z)$ increased with depth. Experiments were repeated for $0.01 \leq Re \leq 1.57$ and $0.09 \leq Fr \leq 6.75$ (figure 2(b)) by varying N and a . As a validation of our averaging procedure, two sets of ten runs were performed in two adjacent observation windows along the settling path, for $a = 196 \mu\text{m}$ and $N = 1.69 \text{ s}^{-1}$. The two resulting curves in (Re, Fr^{-1}) space (curves 1 and 2 in figure 2(b)) are a smooth continuation of each other. For all the settling experiments performed, calculation of dU/dt showed that the added mass and Basset force terms (equation 2.1) contributed less than 1% of the total drag force, justifying our

earlier assumption of quasi-steady settling.

3.2. Wake visualization by Microscale Synthetic Schlieren

To visualize the effect of the settling sphere on the fluid density field, we performed experiments using Microscale Synthetic Schlieren (Yick *et al.* 2006). Synthetic Schlieren is the digital implementation of an optical technique to measure density perturbations using the relation between the density and refractive index of salt-stratified fluid. A detailed description of Microscale Synthetic Schlieren, along with its application to spheres as small as $a = 78 \mu\text{m}$, is presented in Yick *et al.* (2006). Our experiments were performed in a 48 cm high, 6.3 cm long and 2.5 cm wide plexiglas tank, with 0.54 cm thick walls. A stratification was established and measured as described in section 3.1. A three-stage micromanipulator mounted on top of the tank facilitated the accurate deposition of the sphere at the centre of the tank through a conical injector (as above) and subsequent passing through the observation window. The distance between the settling path and the closest wall ($> 32a$) corresponded to a less than 5% change in drag coefficient for a homogeneous fluid (Clift *et al.* 1978): as will be seen below, this is negligible compared to the effect of stratification.

A 2×2 cm mask consisting of a random pattern of $35 \mu\text{m}$ dots was printed on transparency film using a high-resolution image setter (Fineline Imaging, Colorado Springs, CO). The pattern was mounted 8.3 cm behind the back wall of the tank, and imaged at 20 frames/s using a PCO 1600 CCD camera, operating at a resolution of 800×600 pixels. The camera was mounted on a Nikon SMZ 1000 stereomicroscope fitted with a P-Achro 0.5 \times objective, positioned 18.9 cm in front of the mask (the maximum working distance). The apparent displacements of the mask caused by density perturbations due

to the settling sphere were determined by image analysis using Digiflow (2006).

Two forms of processing were used. The first, known as qualitative Synthetic Schlieren, consists simply in subtracting the reference image from each subsequent image and provides a proxy for the relative magnitude of density perturbation gradients. The second, quantitative Synthetic Schlieren, uses cross-correlation algorithms to compute the apparent displacements of the mask and inverts them to obtain the associated gradients in density perturbation. Details of the processing are given in Yick *et al.* (2006). Radial density perturbation gradients $\partial\rho'/\partial r$ were then integrated along r at a given vertical position z , and this was repeated for each of the 600 vertical positions (i.e. 600 vertical pixels) in an image, yielding the density perturbation field ρ' . This was added to the background density field, enabling calculation of isopycnals by contouring the total density field in Matlab.

3.3. Numerical model

Numerical simulations were performed for comparison of the drag coefficient with experimental data and to obtain high resolution information on the density and flow fields over a wide range of parameters. Simulations were carried out in the parameter regime $0.05 \leq Re \leq 2.1$, $0.02 \leq Fr \leq 200$, and $7 \leq Pr \leq 700$. The model was adapted from an earlier one (Torres *et al.* 2000; Larrazábal *et al.* 2003) and is described here only briefly. It considers flow of a linearly stratified fluid at constant velocity U past a stationary sphere (figure 1(a)), and uses finite-differences to solve the nondimensional equations

$$\frac{\partial \mathbf{u}}{\partial t} + \mathbf{u} \cdot \nabla \mathbf{u} = -\nabla p - \frac{\rho'}{Fr^2} \mathbf{j} + \frac{1}{Re} \nabla^2 \mathbf{u}, \quad (3.1)$$

$$\frac{\partial \rho'}{\partial t} + \mathbf{u} \cdot \nabla \rho' = w - 1 + \frac{1}{RePr} \nabla^2 \rho', \quad (3.2)$$

$$\nabla^2 p = -\frac{1}{Fr^2} \nabla \cdot (\rho' \mathbf{j}) - \nabla \cdot [(\mathbf{u} \cdot \nabla) \mathbf{u}] + \frac{1}{Re} \nabla^2 P - \frac{\partial P}{\partial t}, \quad (3.3)$$

obtained by rescaling lengths by a , velocities by U , pressure perturbations by $\rho_0 U^2$, and density perturbations by $-a (d\rho/dz)$. Here $\mathbf{u} = (u, w)$ is the fluid velocity in the radial and vertical direction, respectively, p the pressure, \mathbf{j} the vertical unit vector, positive upwards, and $P = \nabla \cdot \mathbf{u}$. Equation (3.3) replaces the incompressibility condition: when discretizing $\partial P / \partial t$ as $(P^{n+1} - P^n) / \Delta t$ (n refers to the integration time $t = n\Delta t$ and Δt is the integration step), incompressibility was enforced by setting $P^{n+1} = 0$. The boundary conditions on the surface of the sphere were $\mathbf{u} = 0$ and zero density flux, enforced by requiring $(\partial \rho' / \partial z) z + (\partial \rho' / \partial r) r = z$. The surface boundary condition for pressure was obtained from equation (3.1) by setting $\mathbf{u} = 0$. Far from the sphere, all physical quantities tended to their unperturbed values: $\mathbf{u} = (0, 1)$ at the upstream (lower) boundary, $\partial \mathbf{u} / \partial z = 0$ at the downstream (upper) boundary, and $\rho' = \partial p / \partial n = 0$ at both.

To improve accuracy near the sphere surface while simplifying the implementation of boundary conditions, equations (3.1)–(3.3) were written in curvilinear coordinates (ξ, η) and solved on a curvilinear grid (figure 1(b)), as described in Torres *et al.* (2000). The external boundary of the grid was elliptic, with axes lengths of 80 (vertical) and 40 (horizontal). The grid consisted of 65×91 or 195×91 ($\xi \times \eta$) mesh points, non-uniformly distributed with a higher mesh density near the sphere and a smallest grid size of 8.2×10^{-4} . The grid ensured that the density boundary layer $\delta_\rho = O((Re Pr)^{-1/2})$ was accurately resolved: for $Pr = 700$ and $Re = 1$, $\delta_\rho = 0.038$ was covered by 16 grid points. This also ensured resolution of the momentum boundary layer, which was always thicker than the

density boundary layer since $Pr > 1$.

For the small Reynolds number stratified regime investigated here, the GMRES (Generalized Minimal RESidual method) was found to be superior in solving the Poisson equation for pressure (3.3) compared to the Successive Overrelaxation Method (Larrazábal *et al.* 2003) used in a previous version of the code (Torres *et al.* 2000). The solution procedure was then as follows: given \mathbf{u} and ρ at time $t = n \Delta t$, p was obtained from equation (3.3) using GMRES and substituted into equations (3.1) and (3.2). Solution of the latter two equations yielded updated values of \mathbf{u} and ρ at $t = (n + 1) \Delta t$. Equations (3.1)–(3.3) constitute a time-dependent problem, but here we were interested in steady solutions. Therefore, the cycle was repeated starting from a rest configuration $\mathbf{u} = \rho' = 0$ until the convergence criterion $|f^{n+1} - f^n|_{max} < 10^{-4}$ was satisfied, where f represents any one of u , w , p or ρ . The time step was $\Delta t = 0.0025$ or 0.0001 and steady state was typically reached within $t = 30$. Extensive convergence tests on time step and mesh size were carried out by Larrazábal *et al.* (2003).

The drag coefficient C_D^S was computed as the sum of the pressure (C_P^S) and viscous (C_V^S) drag coefficients:

$$C_P^S = -\frac{1}{\frac{1}{2}\rho U^2 \pi a^2} \int_S p \mathbf{n} \cdot \mathbf{j} dS, \quad (3.4)$$

$$C_V^S = \frac{1}{\frac{1}{2}\rho U^2 \pi a^2} \int_S \mu \mathbf{n} \cdot ((\nabla \mathbf{u}) + (\nabla \mathbf{u})^T) \cdot \mathbf{j} dS, \quad (3.5)$$

where \mathbf{n} is the unit vector normal to the sphere surface S , positive outward. Drag coefficients were normalized by their homogeneous counterparts to obtain the normalized drag coefficients C_D^N , C_P^N and C_V^N .

4. Results

We begin by reporting experimental results for particles released in homogeneous salt-water solutions. Unless otherwise noted, all results are expressed in dimensionless form as described in section 3.3. Using the measured terminal settling velocity U , C_D^H was computed from a balance of buoyancy and drag (equation 2.4, for C_D^H instead of C_D^S). This was repeated for four fluid densities. Results are reported as a function of Re in figure 3 and compared to the prediction from equation (2.2). The good agreement validates our procedure for measuring settling velocity, ensuring that drag coefficients can be reliably determined. A validation of the numerical model was performed by computing C_D^S for various Re and $Fr = 200$. At this high value of Fr , stratification is unimportant and as one would expect the calculated values of C_D^S tend to C_D^H (figure 3).

We proceeded to measure drag in a linearly stratified fluid and present results in terms of the normalized drag coefficient C_D^N . This is shown as a function of Fr^{-1} and Ri in figures 4(a,b), respectively. The choice of Fr^{-1} as the independent parameter is appropriate at moderate Re (Torres *et al.* 2000; Higginson *et al.* 2003), while Ri is suggested by the theoretical analysis of Zvirin & Chadwick (1974). Three important conclusions emerge. The first is that $C_D^N > 1$, demonstrating that a linear stratification does increase drag at small Re ; indeed, our experiments reveal that stratified drag can be more than three-fold greater than its homogeneous counterpart. Secondly, C_D^N increases monotonically with both Fr^{-1} and Ri , showing that stronger stratifications result in larger drag. Thirdly, the data collapses considerably better when plotted against Ri than against Fr^{-1} , implying that Re and Fr affect C_D^N only through the combination $Ri = Re/Fr^2$ at small Re . We found a fit of the form $1 + \alpha Ri^q$ appropriate to describe the dependence of C_D^N on Ri ,

with the best fit for the experiments given by $C_D^N = 1 + 1.95 Ri^{0.62}$.

Drag coefficients were also computed numerically. We performed two sets of simulations ($Re = 0.05$ and 0.5) at $Pr = 700$ to model a salt stratification (the data set for $Pr = 7$ represents a temperature stratification and will be discussed later). Numerical results (figure 4) confirm that $C_D^N > 1$ and there is good quantitative agreement with the experiments. Furthermore, numerical results likewise reveal the clear dependence of C_D^N on Ri by successfully collapsing data for two different Re . A best fit to the combined numerical data for $Re = 0.05$ and 0.5 yields $C_D^N = 1 + 1.91 Ri^{0.41}$ ($C_D^N - 1 \sim Ri^{0.39}$ for $Re = 0.05$; $C_D^N - 1 \sim Ri^{0.43}$ for $Re = 0.5$). This is a slightly weaker dependence compared to the experiments, but the difference in C_D^N predicted from the two fits is $< 15\%$ over the experimental parameter range.

Numerical results further reveal that both the pressure and viscous components of drag increase with Ri (figures 4(c,d)). For $Ri = 0$, $C_P^N = 1/3$ and $C_V^N = 2/3$, as expected for Stokes flow. The scaling of $C_P^N - 1/3$ and $C_V^N - 2/3$ with Ri is similar to $C_D^N - 1$, with a slightly larger exponent for C_P^N . To understand the origin of pressure and viscous drag increase, in figures 5(a,b) we plot the pressure and the vertical component of the tangential shear stress along the surface of the sphere, respectively, corresponding to the integrands in equations (3.4)–(3.5). An increase in Ri induces a larger front-aft pressure difference (figure 5(a)), resulting in increased pressure drag, and enhances shear stresses, particularly at the equator (figure 5(b)), accounting for the larger viscous drag.

Further detail on the nature of the wake behind a settling sphere was obtained using Microscale Synthetic Schlieren. Figure 6 shows a qualitative Synthetic Schlieren image

for an $a = 390 \mu\text{m}$ sphere settling in a stratification with $N = 1.31 \text{ s}^{-1}$ (corresponding to $Re = 2.1$, $Fr = 10.2$, $Ri = 0.02$). As described by Yick *et al.* (2006), due to the limited depth of focus of the microscope, the position of the sphere is known to within one sphere radius. Several features of the wake are immediately apparent. It is symmetric about the central axis, as one would expect from radial symmetry, and is of considerable length ($> 22 \text{ mm}$), revealing that the stratification remains perturbed far downstream of the sphere. The wake structure becomes more complex near its end, in the form of a pair of faint white lobes.

Quantitative processing of this data yields the density field in the wake of the sphere (figure 7(a)). Isopycnals are dragged down by as much as five sphere radii. Vertical isopycnal displacement diminishes with distance z downstream of the sphere, as isopycnals return to their neutral buoyancy position. As the viscous force resisting this retreat decreases with both z and r , retreating isopycnals overshoot on the rim of the wake at $z \sim 20$, creating a toroidal structure akin to that of a laminar buoyant jet (Tenner & Gebhart 1971). This mild overshoot, which is responsible for the white lobes in figure 6, is locally damped by viscosity and does not trigger internal waves.

Several key features of the wake are confirmed by the numerical density field, shown in figure 7(b). The wake length is similar for experiments and numerics, and in both cases isopycnals overshoot without radiating internal waves. The deformation of numerical isopycnals is somewhat sharper compared to experiments, for reasons that we could not determine. Several possibilities were tested and discounted, including the resolution of the camera, random dot pattern, Schlieren processing and numerical grid. It is interesting, however, that drag coefficients are in good agreement (figure 4). Added drag will

later be rationalized in terms of the buoyancy of fluid in the immediate vicinity of the sphere. In this region, isopycnal distortion in experiments and numerics is comparable.

Taking a closer look at the numerical results in the vicinity of the sphere, we see that isopycnals are strongly compressed in front of the sphere (figure 8(a)), resulting in an increased pressure gradient (figure 5(a)) and hence pressure drag (figure 4(c)). As the sphere descends, isopycnals make way and tilt (figure 8(b)), causing baroclinic generation of vorticity, which enhances shear stresses (figure 5(b)) and thus viscous drag (figure 4(d)). At the rear, isopycnals detach from the sphere, however without generating the buoyant jet (figure 8(c)) characteristic of higher Re (Torres *et al.* 2000). On the larger scale, simulations predict that wake length and isopycnal deflection decrease with increasing Ri (figure 9), since enhanced buoyancy more effectively opposes vertical motion and more rapidly restores isopycnals. These features of the numerical solution are supported by further experimental observations. As shown in figure 10(a), the only region where Synthetic Schlieren detected vertical pattern displacements (corresponding to vertical density gradients) was ahead of the sphere, in contrast to the strong horizontal pattern displacements that were detected in the wake (figure 10(b)). Furthermore, the length of the wake and the magnitude of isopycnal distortion both clearly diminished as Ri increased (figure 10(b,c)).

5. Discussion

The primary result of this study is that stratification increases hydrodynamic drag on a sphere settling at small Re : both experiments and numerical simulations revealed that $C_D^N > 1$. For a given stratifying agent (i.e. Pr), the drag increase is best characterized by $Ri = Re/Fr^2$. The latter arises naturally when considering the relative importance of

buoyancy and viscous forces, which can be expressed as $\int_{V_F} g \Delta \rho dV / \int_{S_F} \mu (\partial w / \partial r) dS$, where V_F and S_F are the volume and surface area of a fluid element; assuming that lengths scale with a , speeds with U and density contrast with $a (d\rho/dz)$, this ratio scales like Ri . The experimentally and numerically determined drag coefficients are in good quantitative agreement (figure 4(b)), reaching up to 3.4 times the homogeneous value for $0 < Ri < 2$. To further increase Ri while maintaining Re small, N would have to be increased beyond our maximum value of 2.92 s^{-1} ; such large values are rare in nature. Considering both experimental and numerical results, our study suggests that the normalized drag coefficient scales as $C_D^N - 1 \sim Ri^q$, where $q = 0.51 \pm 0.11$, in contrast to the theoretical prediction $q = 1/3$ for $Ri \ll 1$ (Zvirin & Chadwick 1974).

The observed added drag due to stratification at small Re complements earlier studies at higher Re (Srđić-Mitrović *et al.* 1999; Torres *et al.* 2000; Higginson *et al.* 2003) and it is worthwhile to assess whether previously proposed mechanisms can account for our findings. For a linear stratification at $25 \leq Re \leq 100$, Torres *et al.* (2000) found that the increase in drag of a settling sphere was related to a rear buoyant jet; the current numerical studies, however, reveal no sign of such a jet (figure 8(c)), consistent with the increased importance of viscous forces, which prevent a rapid retreat of isopycnals. For a step-wise stratification at $1.5 < Re < 15$, Srđić-Mitrović *et al.* (1999) found that the increased drag on a sphere was accounted for by the buoyancy in the entire wake of dragged-down fluid. In our case, integration of the buoyancy over the entire wake in figure 7(a) results in a force ($13.0 \times 10^{-8} \text{ N}$) far larger than the measured increase in drag ($1.5 \times 10^{-8} \text{ N}$). That drag does not depend on the entire wake is further supported by the numerical results in two manners. Firstly, two wakes can have significantly different size (figure 11), hence buoyancy, and yet the same drag coefficient (figure 4). Secondly,

a force balance on the wake that ignores the contribution of the sphere yields a scaling argument that successfully predicts its width W . The balance between viscous and buoyancy forces suggests $(\mu U/W) W^2 \sim g \Delta \rho W^3$, where $\Delta \rho \sim N^2 \rho_0 W/g$ and vertical isopycnal deflections are assumed to also scale with W . This yields $W/a \sim Ri^{-1/3}$, which is borne out by the numerical results in figure 13(a), where W was taken as the distance from the axis of symmetry to the point where vertical isopycnal deflection decreased to $0.1a$.

Instead, we propose that it is the buoyancy of a localized fluid region around the sphere that determines the added drag. This is related to the work by Higginson *et al.* (2003) at higher Re ($\sim O(10^3)$), where added drag on a rising grid of bars was found to derive from the buoyancy of fluid in the drift volume. In our case, the fluid volume affecting drag can be identified by considering the vertical velocity field w (figure 12(b)), which reveals that the wake is composed of two distinct regions: a lower one surrounds the sphere and descends at nearly its same speed ($w \sim -1$), dragged down by viscous shear forces; the upper one ascends slowly ($w > 0$), due to isopycnals retreating under the effect of buoyancy. It is then reasonable to hypothesize that the buoyancy of the fluid immediately adjacent to the sphere is responsible for the added drag, while the rest of the wake is simply a remnant of the sphere's passage.

Here we rationalize the added drag by a scaling argument based on the buoyancy of a fluid region dragged down by the sphere. For clarity, a dimensional formulation is adopted. Assuming a spherical shell of width δ , the volume of this region scales as $\pi a^2 \delta$, while its density contrast is $\Delta \rho = H \, d\rho/dz$, where H is the maximum distance an isopycnal is dragged down. The normalized drag coefficient can then be written as the

ratio of this buoyancy force and the homogeneous drag force,

$$C_D^N - 1 \sim \frac{\pi a^2 \delta g \Delta \rho}{C_D^H \frac{1}{2} \rho U^2 \pi a^2} \sim \frac{1}{Fr^2} \frac{1}{C_D^H} \frac{\delta}{a} \frac{H}{a}, \quad (5.1)$$

where δ/a and H/a are still to be determined.

We propose that $\delta \sim (\nu/N)^{1/2}$, the natural length scale in a viscous and buoyant flow (Basak & Sarkar 2006; Blanchette *et al.* 2008), resulting in $\delta/a \sim (Fr/Re)^{1/2}$. This was indeed the scaling of the extent of the fluid shell around the sphere in our numerical data (figure 13(b)), for which δ was operationally defined as the thickness of the region where $\Delta\rho$ was $> 5\%$ of its maximum value, which occurred at the sphere surface. On the other hand, despite considering several possibilities, we were unable to find an *a priori* scaling for H . At higher Re ($\sim O(10^3)$), $H/a \sim Fr$ as a result of a balance between kinetic and potential energy (Higginson *et al.* 2003), yet this is not applicable in our regime where viscous dissipation is important. Hence, we resorted to an empirical scaling, by computing H from simulations as the maximum isopycnal deflection immediately upstream of the sphere ($z = -a$). Figure 13(c) shows that $H/a \sim Fr^{1/2}$, in line with our earlier observation that isopycnal deflection decreases with increasing stratification. The residual Re dependence in figure 13(c) is very weak ($\sim Re^{1/10}$) and will be neglected.

With the aforementioned scalings, and using $C_D^H \sim 1/Re$ (appropriate for small Re), equation (5.1) reduces to $C_D^N - 1 \sim Ri^{1/2}$. This compares favourably with our result $C_D^N - 1 \sim Ri^q$, where $q = 0.62$ from experiments, $q = 0.41$ from numerics, for an average of $q = 0.51$. These results suggest a new expression for the drag coefficient in a salt-stratified ambient,

$$C_D^S = \left(\frac{12}{Re} + \frac{6}{1 + \sqrt{2Re}} + 0.4 \right) (1 + \alpha Ri^{1/2}), \quad (5.2)$$

where $\alpha = 1.9$ ($\alpha = 1.95$ and 1.91 in experiments and numerics, respectively). This rationalization of the added drag also applies to the moderate Re regime, where the dragged-down region scales with the drift volume ($\sim a^3$), $H/a \sim Fr$ (Higginson *et al.* 2003), and $C_D^H \sim Re^0$; resulting in $C_D^N - 1 \sim Fr^{-1}$, which is verified by analysis of the data in Torres *et al.* (2000) and is in agreement with Higginson *et al.* (2003).

In general, the problem of a sphere settling through a stratified fluid further depends on Pr . While our study focused on salt-stratifications ($Pr = 700$), the case of a thermal stratification ($Pr = 7$) is also of relevance in aquatic environments. For this case, simulations show a smaller increase in drag due to stratification (figure 4) and a weaker dependence on Ri ($q = 0.29$). This can be rationalized by considering that stronger diffusion more effectively counteracts the accumulation of buoyancy forces by more rapidly smoothing out isopycnal deflections. This is shown in figure 14, which compares the wake for $Pr = 7, 100$ and 700 : isopycnal deflections decrease with Pr (see also figure 13(c)) and the wake becomes shorter and wider (see also figure 13(a)).

The observed added drag implies that a sphere settles more slowly in a stratified fluid than predicted using homogeneous-fluid formulations. Figure 15(a) shows the experimental trajectory of an $a = 196 \mu\text{m}$ sphere in a stratification with $N = 1.69 \text{ s}^{-1}$, compared to its expected trajectory in a homogeneous fluid. The distance traveled over 100 s is roughly half in the stratified case, and is predicted to within 10% by our drag coefficient formulation (5.2). How important is this effect in natural stratified environments? Some of the strongest aquatic stratifications are found in inlets, fjords and river outflows, where freshwater overlying saltier water can result in N being as large as 0.2 s^{-1} (Farmer & Armi 1999, figure 2A). While freshwater lakes can be nearly as strongly stratified due to

temperature (Patterson *et al.* 1984; King *et al.* 1999), the corresponding Prandtl number is much smaller and the influence of stratification therefore reduced. Heading further out into the ocean, density gradients are generally weaker, reaching maximum values on the order of $N \sim 0.02 \text{ s}^{-1}$. The role of salt-stratifications was investigated by plotting the ratio of stratified to homogeneous travel time (figure 15(b)); these were found by integrating the settling speed U , determined numerically from equation (2.3) using the stratified (equation 5.2) and homogeneous (equation 2.2) drag coefficients. This procedure was repeated for a range of particle sizes up to $a = 2500 \text{ }\mu\text{m}$ and three values of the density contrast $\Delta\rho = 1, 5$ and 20 kg m^{-3} , representative of biological matter. The effect of stratification increases with particle size, as expected from the Ri dependence. In the open ocean we predict the increase in settling time due to stratification is $< 6\%$, rising significantly to 66% for strongly stratified fjords and inlets. This suggests that the effect of stratification on settling time needs to be accounted for in strongly stratified natural water bodies. We expect this effect to be compounded by hindered settling due to particle-particle interactions in particle clouds (Bush *et al.* 2003; Blanchette & Bush 2005).

6. Conclusions

We have presented a combined experimental and numerical investigation of the fluid mechanics of a sphere settling in a linearly stratified fluid at small Reynolds numbers. This study provides the first experimental evidence of stratification-induced enhanced drag in a continuously stratified fluid at small Re , further supported by numerical simulations. The increase in drag is governed by a single dimensionless parameter, the Richardson number, expressing the relative importance of buoyancy and shear forces. The normalized drag coefficient C_D^N was found to scale like $1 + 1.9 Ri^{0.51}$, with a small discrepancy in

the exponent (± 0.1) between numerics and experiments. Microscale Synthetic Schlieren revealed that a particle's signature lingers long after it has passed, producing an extended wake in which density is perturbed. Careful analysis of the flow and density fields showed that only a minor portion of the wake is responsible for the added drag, enabling us to rationalize observations via a scaling argument. The added drag decreases with Pr , as diffusion increasingly counteracts buoyancy. This effect is relevant to strongly stratified aquatic environments (e.g. inlets and fjords, and to a lesser extent the open ocean and lakes), where it can enhance retention of biological material at density interfaces (MacIntyre *et al.* 1995) and colonization of marine snow aggregates by microorganisms (Stocker *et al.* 2008), ultimately affecting vertical fluxes of matter in biogeochemical cycles.

7. Acknowledgments

We would like to thank John Bush, Paul Linden and Francois Blanchette for helpful discussions, Stuart Dalziel for access to Digiflow and Zheng Gong for assistance with experiments. This work was partially supported by NSF grant OCE-0526241 to RS. Computer time for simulations was provided by the Multidisciplinary Center of Scientific Visualization and Computing, University of Carabobo, Venezuela.

REFERENCES

- ABAID, N., ADALSTEINSSON, D., AGYAPONG, A. & McLAUGHLIN, R.M. 2004 An internal splash: Levitation of falling spheres in a stratified fluid. *Phys. Fluids* **16**, 1567.
- BASAK, S. & SARKAR, S. 2006 Dynamics of a stratified shear layer with horizontal shear. *J. Fluid Mech.* **568**, 19–54.
- BLANCHETTE, F. & BUSH, J.W.M. 2005 Particle concentration evolution and sedimentation-induced instabilities in a stably stratified environment. *Phys. Fluids* **17**, 073302.

- BLANCHETTE, F., PEACOCK, T. & COUSIN, R. 2008 Stability of a stratified fluid with a vertically moving side-wall. *J. Fluid Mech.* **609**, 305–317.
- BUSH, J.W.M., THURBER, B.A. & BLANCHETTE, F. 2003 Particle clouds in homogeneous and stratified environments. *J. Fluid Mech.* **489**, 29–54.
- CLIFT, R., GRACE, J.R. & WEBER, M.E. 1978 *Bubbles, Drops, and Particles*, 380 pp. Academic Press.
- DALZIEL, S.B. 1992 Decay of rotating turbulence: some particle tracking experiments. *Appl. Scien. Res.* **49**, 217–244.
- DIGIFLOW 2006 www.damtp.cam.ac.uk/lab/digiflow.
- EAMES, I., GOBBY, D. & DALZIEL, S.B. 2003 Fluid displacement by Stokes flow past a spherical droplet. *J. Fluid Mech.* **485**, 67–85.
- FARMER, D. & ARMI, L. 1999 The generation and trapping of solitary waves over topography. *Science* **283**, 188–190.
- FOFONOFF, P. & MILLARD, R.C. JR 1983 Algorithms for computation of fundamental properties of seawater. *Unesco Tech. Pap. Mar. Sci.* **44**, 53.
- GREENSLADE, M.D. 1994 Strongly stratified airflow over and around mountains. In *Stably Stratified Flows: Flow and Dispersion over Topography, Proc. 4th IMA Conf. on Stably Stratified Flows, University of Surrey, Sept. 1992*, eds. I.P. Castro and N.J. Rockliff, Oxford University Press .
- GREENSLADE, M.D. 2000 Drag on a sphere moving horizontally in a stratified fluid. *J. Fluid Mech.* **418**, 339–350.
- HIGGINSON, R.C., DALZIEL, S.B. & LINDEN, P.F. 2003 The drag on a vertically moving grid of bars in a linearly stratified fluid. *Expts. Fluids* **34**, 678–686.
- KELLOG, W.N. 1990 Aerosols and climate. In *Interaction of Energy and Climate*, eds. W. Bach, J. Pankrath and J. Williams. Reidel .
- KING, J.R., SHUTER, B.J. & ZIMMERMAN, A.P. 1999 Signals of climate trends and extreme events in the thermal stratification pattern of multibasin Lake Opeongo, Ontario. *Can. J. Fish. Aquat. Sci.* **56**, 847–852.

- LARRAZÁBAL, G., TORRES, C.R. & CASTILLO, J. 2003 An efficient and robust algorithm for 2D stratified fluid flow calculations. *Appl. Num. Math.* **47**, 493–502.
- LEAL, L.G. 1980 Particle motions in a viscous fluid. *Ann. Rev. Fluid Mech.* **12**, 435–476.
- LOFQUIST, K.E.B. & PURTELL, L.P. 1984 Drag on a sphere moving horizontally through a stratified liquid. *J. Fluid Mech.* **148**, 271–284.
- MACINTYRE, S., ALLDREDGE, A.L. & GOTSCHALK, C.C. 1995 Accumulation of marine snow at density discontinuities in the water column. *Limnol. Oceanogr.* **40**, 449–468.
- OCHOA, J.L. & Van Woert, M.L. 1977 Flow visualization of boundary layer separation in a stratified fluid. *Unpublished report, Scripps Institution of Oceanography* **28**.
- OSTER, G. 1965 Density gradients. *Sci. Am.* **213**, 70.
- PATTERSON, J.C., HAMBLIN, P.F. & IMBERGER, J. 1984 Classification and dynamic simulation of the vertical density structure of lakes. *Limnol. Oceanogr.* **29**, 845–861.
- SCASE, M.M. & DALZIEL, S.B. 2004 Internal wave fields and drag generated by a translating body in a stratified fluid. *J. Fluid Mech.* **498**, 289–313.
- SMITH, R.B. 1979 The influence of mountains on the atmosphere. *Advances in Geophysics*, Vol. 21. New York: Academic Press.
- SMITH, R.B. 1980 Linear theory of stratified hydrostatic flow past an isolated mountain. *Tellus* **32**, 348–364.
- SRDIĆ-MITROVIĆ, A.N., MOHAMED, N.A. & FERNANDO, J.S. 1999 Gravitational settling of particles through density interfaces. *J. Fluid Mech.* **381**, 175–198.
- STOCKER, R., SEYMOUR, J.R., SAMADANI, A., HUNT, D.E. & POLZ, M.F. 2008 Rapid chemotactic response enables marine bacteria to exploit ephemeral microscale nutrient patches. *Proc. Natl. Acad. Sci.* **105**, 4209–4214.
- TENNER, A.R. & GEBHART, B. 1971 Laminar and axisymmetric vertical jets in a stably stratified environment. *Int. J. Heat Mass Transfer* **14**, 2051–2062.
- TORRES, C.R., HANAZAKI, H., OCHOA, J., CASTILLO, J. & Van Woert, M. 2000 Flow past a sphere moving vertically in a stratified diffusive fluid. *J. Fluid Mech.* **417**, 211–236.
- TRITTON, D.J. 1988 *Physical Fluid Mechanics*, 2nd ed, 519 pp. Oxford University Press.

- TURCO, R.P., TOON, O.B., ACKERMAN, T.P., POLLACK, J.B. & SAGAN, C. 1990 Climate and smoke: An appraisal of nuclear winter. *Science* **247**, 166–176.
- VOSPER, S.B., CASTRO, I.P., SNYDER, W.H. & MOBBS, S.D. 1999 Experimental studies of strongly stratified flow past three-dimensional orography. *J. Fluid Mech.* **390**, 223–249.
- WARREN, F.W.G. 1960 Wave resistance to vertical motion in a stratified fluid. *J. Fluid Mech.* **7**, 209–229.
- WHITE, F.M. 2005 *Viscous Fluid Flow*, 3rd ed., 640 pp. McGraw-Hill.
- YICK, K.Y., STOCKER, R. & PEACOCK, T. 2006 Microscale synthetic schlieren. *Expts. Fluids* **42**, 41–48.
- YIH, C.S. 1980 *Stratified Flows*, 2nd ed., 458 pp. Academic Press.
- ZVIRIN, Y. & CHADWICK, R.S. 1974 Settling of an axially symmetric body in a viscous stratified fluid. *Int. J. Multiph. Flow* **1**, 743–752.

Figure captions

Figure 1. (a) Schematic of a sphere settling in a linearly stratified fluid. (b) The numerical grid in the region close to the sphere.

Figure 2. (a) The settling velocity U versus depth z for ten replicate experiments (faint lines), along with the mean (bold line), for $a = 390 \mu\text{m}$ and $N = 2.92 \text{ s}^{-1}$. (b) The parameter regime explored experimentally, shown in terms of Re and Fr^{-1} . Each experiment is represented by a continuous curve, because a particle samples decreasing Re and Fr as it settles into progressively denser fluid. Curves at larger Fr are shorter because in a weaker stratification U (and thus Re and Fr) varies less over a given vertical window. All experiments were conducted at $Pr = 700$ (salt stratification). Two sphere sizes were used: $a = 196 \mu\text{m}$ (experiments 1,2,3,5,6,9,10) and $a = 390 \mu\text{m}$ (experiments 4,7,8,11).

Figure 3. The homogeneous drag coefficient C_D^H measured experimentally (circles) and computed numerically (triangles), compared with the prediction from equation (2.2) (continuous line), as a function of Re .

Figure 4. The normalized drag coefficient C_D^N as a function of Fr^{-1} for experiments (solid blue lines) and numerical simulations (symbols). The bars represent upper and lower bounds of experimental values. (b) C_D^N as a function of Ri for experiments (solid blue lines) and simulations (symbols). Dashed lines represent power law fits, performed separately for the experiments and each set of simulations, and color-coded accordingly. Inset: detail of $C_D^N - 1$ vs. Ri in log-log scale. (c, d) The numerical pressure drag coefficient C_P^N and viscous drag coefficient C_V^N vs. Ri , along with best fit power laws (dashed lines). In all panels, dotted lines represent the theoretical prediction for homogeneous

Stokes flow ($Ri = 0$): $C_D^N = 1$, $C_P^N = 1/3$ and $C_V^N = 2/3$.

Figure 5. (a) Pressure and (b) vertical component of the tangential shear stress, along the surface of a settling sphere for $Re = 0.05$ and different Ri . $Ri = 0.29, 0.43, 0.61, 0.84, 1.12, 1.45$ from top to bottom in panel (a), and from bottom to top in panel (b). $\theta = -\pi/2$ is the front of the sphere (figure 1).

Figure 6. Qualitative Synthetic Schlieren visualization of the wake of an $a = 390 \mu\text{m}$ sphere for $N = 1.31 \text{ s}^{-1}$. The intensity is correlated with the magnitude of the density perturbation gradient. The figure is a composite of two frames (top and bottom) and the position of the sphere, added in postprocessing, is accurate to within one sphere radius. Adapted from Yick *et al.* (2006).

Figure 7. Dimensionless density field $\rho - \rho(0)$ in the wake of a settling sphere for $Ri = 0.02$ ($Re = 2.1, Fr = 10.2$) obtained from (a) Microscale Synthetic Schlieren and (b) numerical simulation.

Figure 8. (a, b) Numerical isopycnal distortion at two locations around the sphere. Colorbars show $\rho - \rho(0)$. (c) Numerical velocity field behind the sphere. For all cases, $Ri = 0.29$ ($Re = 0.05, Fr = 0.42$).

Figure 9. Numerical density field $\rho - \rho(0)$ in the wake of a settling sphere for (a) $Ri = 0.29$ ($Re = 0.05, Fr = 0.42$) and (b) $Ri = 1.45$ ($Re = 0.05, Fr = 0.19$). Higher Ri corresponds to a shorter wake and smaller isopycnal deflections.

Figure 10. (a) Horizontal and (b,c) vertical pattern displacements generated by an $a = 390 \mu\text{m}$ settling sphere, detected using Microscale Synthetic Schlieren. Colorbar units are in pixels. (a,b) $N = 1.31 \text{ s}^{-1}$ ($Ri = 0.02, Re = 2.1, Fr = 10.2$); (c) $N = 2.50 \text{ s}^{-1}$ ($Ri = 0.89, Re = 0.15, Fr = 0.4$). The position of the sphere, added in postprocessing, is accurate to within one sphere radius. Note the different colorbar scale in (b) and (c).

Figure 11. Numerical density field $\rho - \rho(0)$ in the wake of a settling sphere for $Ri = 0.43$ obtained from (a) $Re = 0.05, Fr = 0.34$ and (b) $Re = 0.5, Fr = 1.08$. Note the strong difference in the wake structure, except in the region closest to the sphere.

Figure 12. (a) The width of the wake W as a function of $Ri^{-1/3}$. (b) The length scale δ of the fluid region responsible for the added drag, as a function of $(Fr/Re)^{1/2}$. (c) The maximum isopycnal deflection H as a function of $Fr^{1/2}$. W , δ and H were computed from numerical simulations as described in the text and nondimensionalized by a .

Figure 13. (a) Density contrast $\Delta\rho$ and (b) vertical fluid velocity w in the wake of a settling sphere for $Ri = 0.29$ ($Re = 0.05, Fr = 0.42$). The long wake (panel a) comprises two distinct regions (panel b): the lower one travels at a speed comparable to that of the sphere ($w \sim -1$).

Figure 14. Numerical density field $\rho - \rho(0)$ for (a) $Pr = 7$, (b) $Pr = 100$, (c) $Pr = 700$. In all panels, $Ri = 1.25$ ($Re = 0.05, Fr = 0.2$).

Figure 15. (a) Trajectory of an $a = 196 \mu\text{m}$ sphere settling in stratified fluid with

$N = 1.69 \text{ s}^{-1}$, determined experimentally (solid line) and predicted using the stratified drag coefficient from equation (5.2) (dashed line). Also shown is the trajectory of the same particle assuming a locally homogeneous drag formulation, equation (2.2) (dotted line). (b) The ratio of travel times computed using a stratified drag coefficient versus a locally homogeneous one, as a function of particle size a , density contrast $\Delta\rho$ and stratification N .

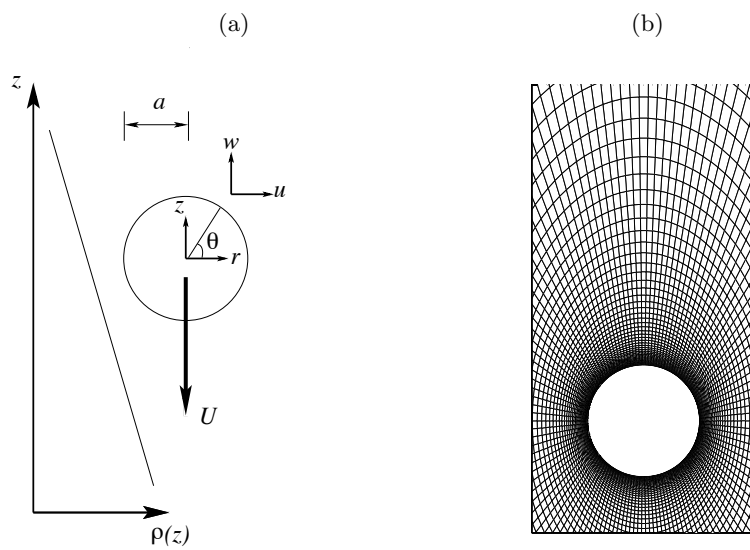


FIGURE 1.

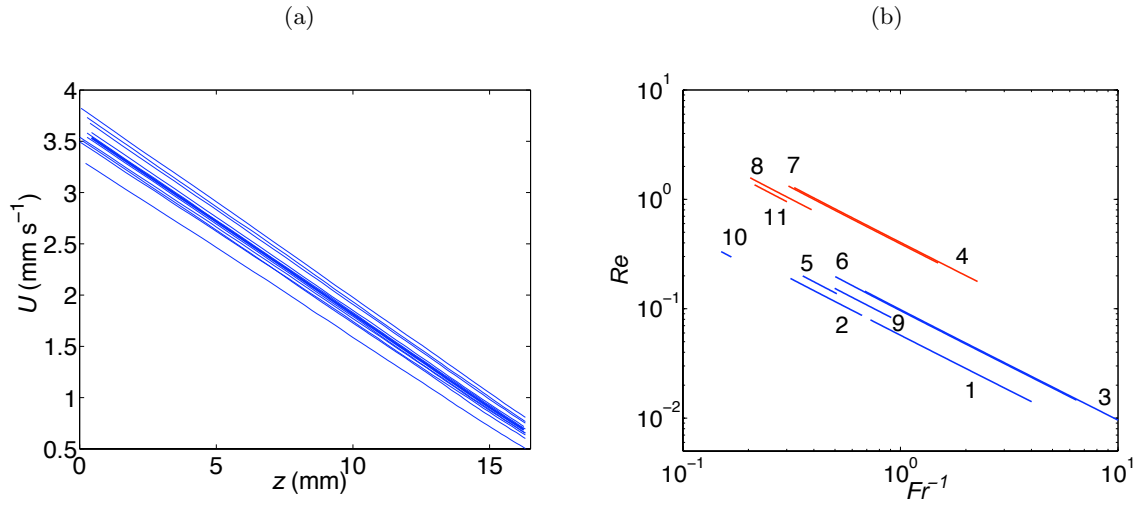


FIGURE 2.

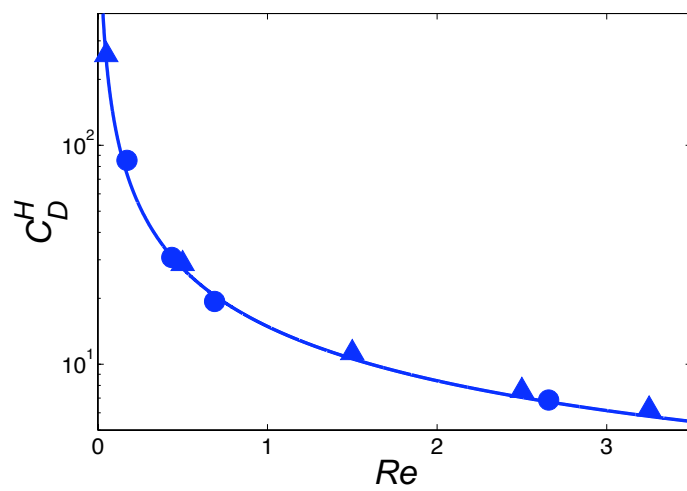
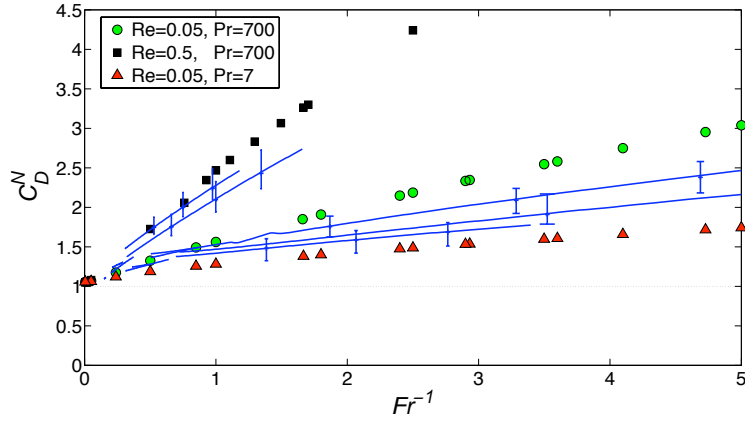
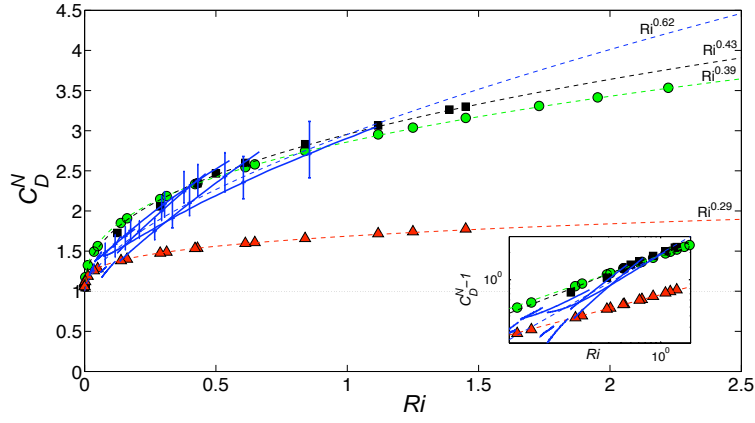


FIGURE 3.

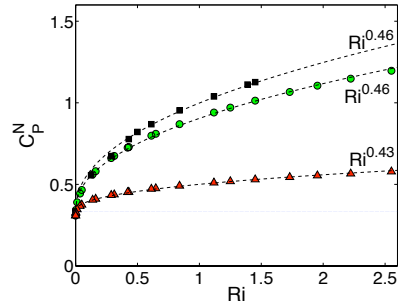
(a)



(b)



(c)



(d)

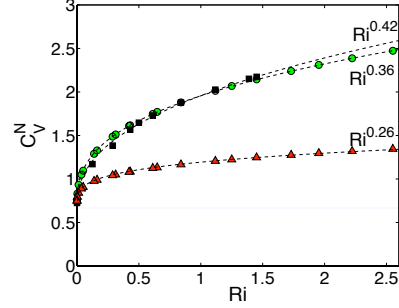


FIGURE 4.

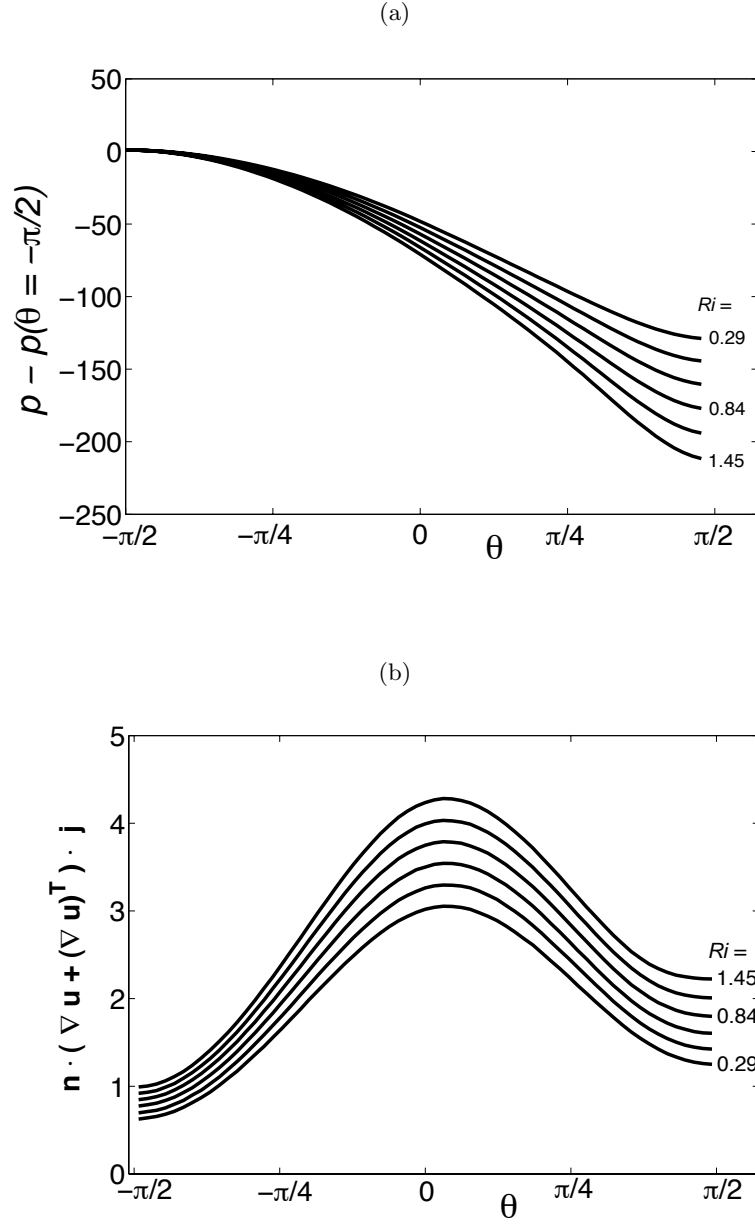


FIGURE 5.

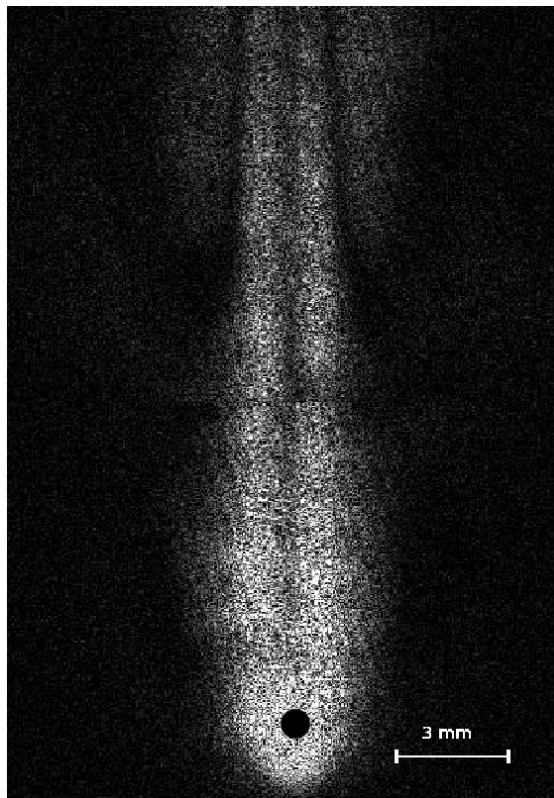


FIGURE 6.

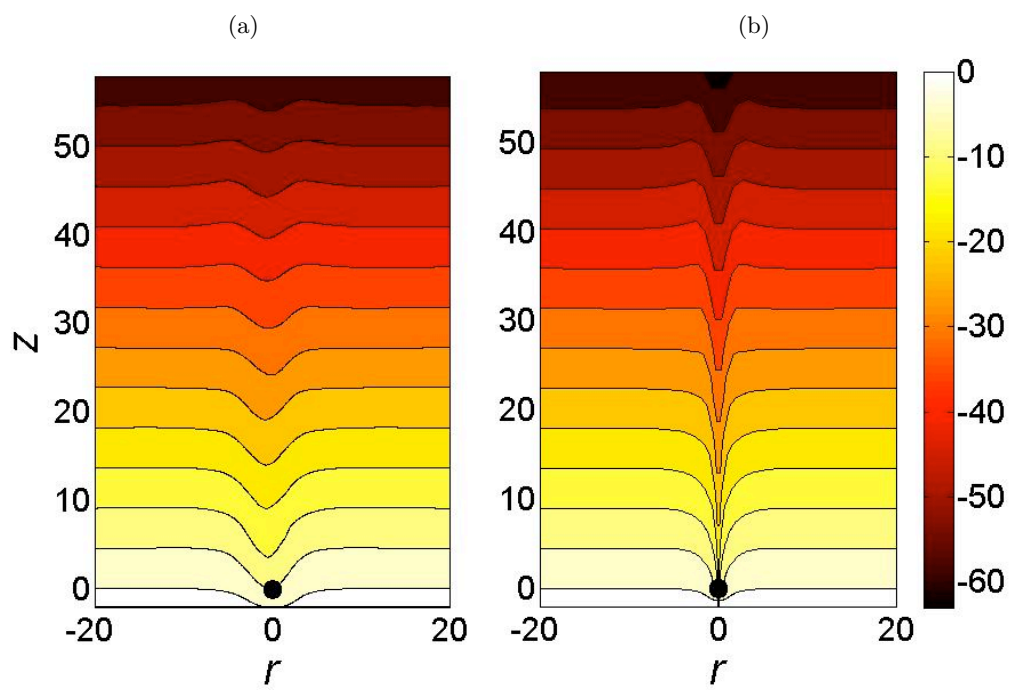


FIGURE 7.

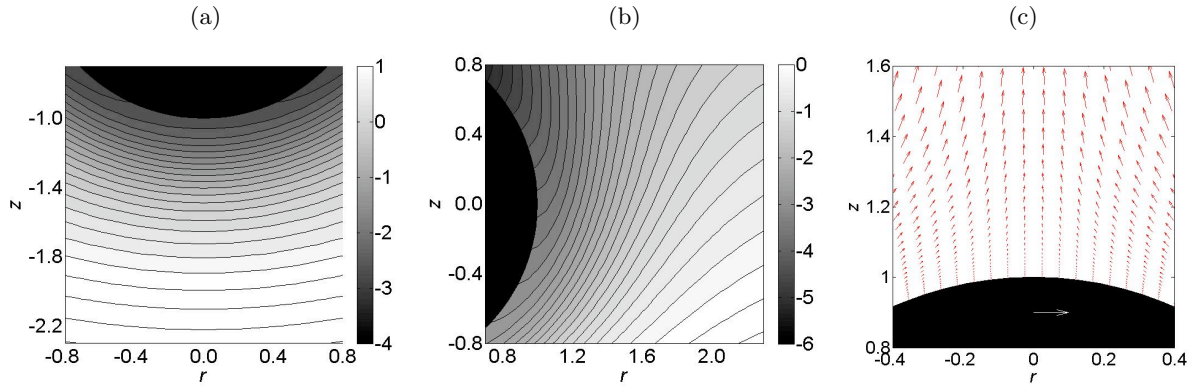


FIGURE 8.

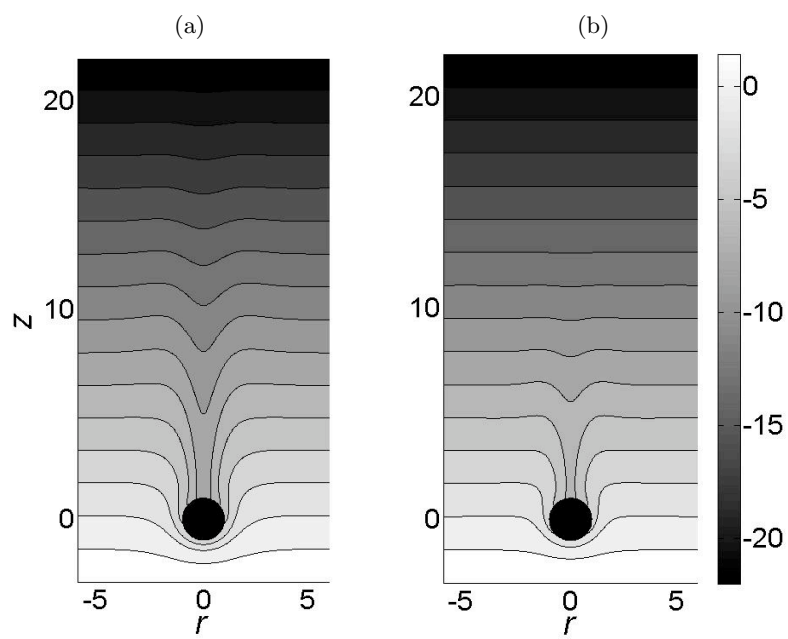


FIGURE 9.

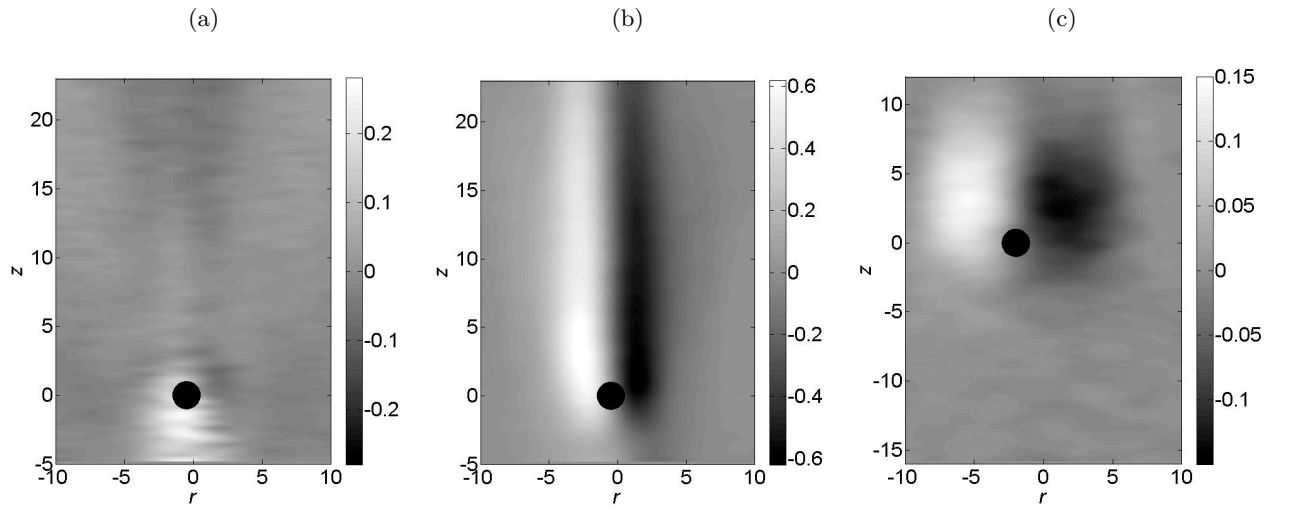


FIGURE 10.

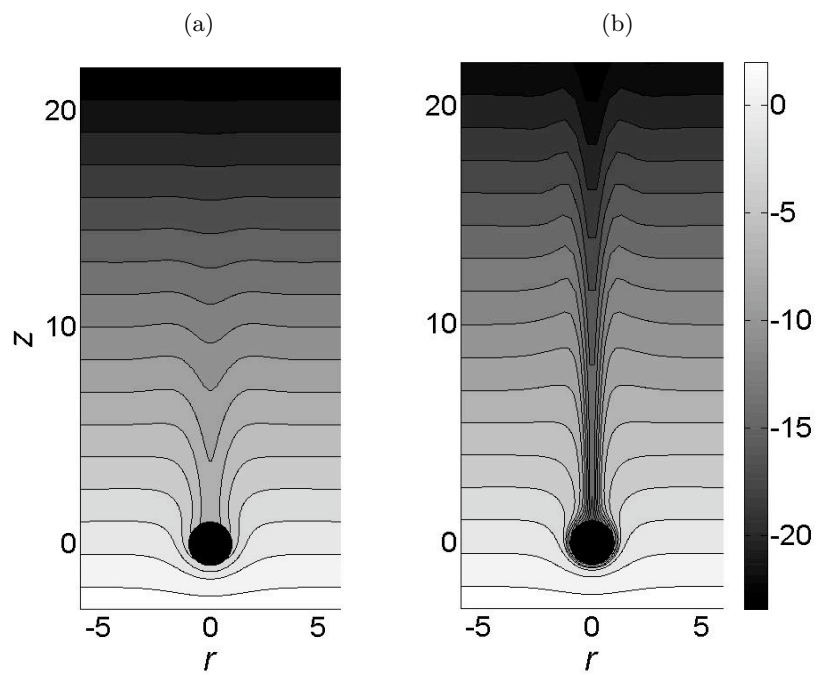


FIGURE 11.

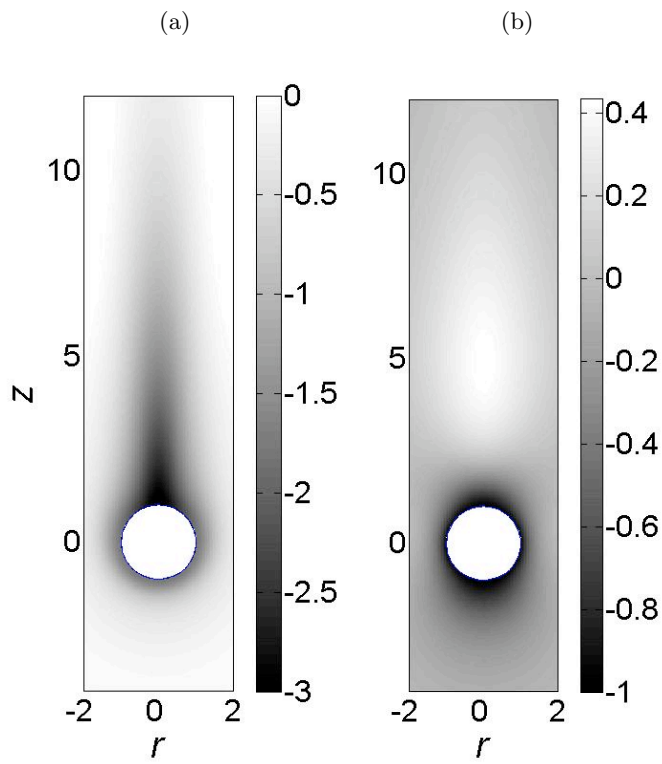


FIGURE 12.

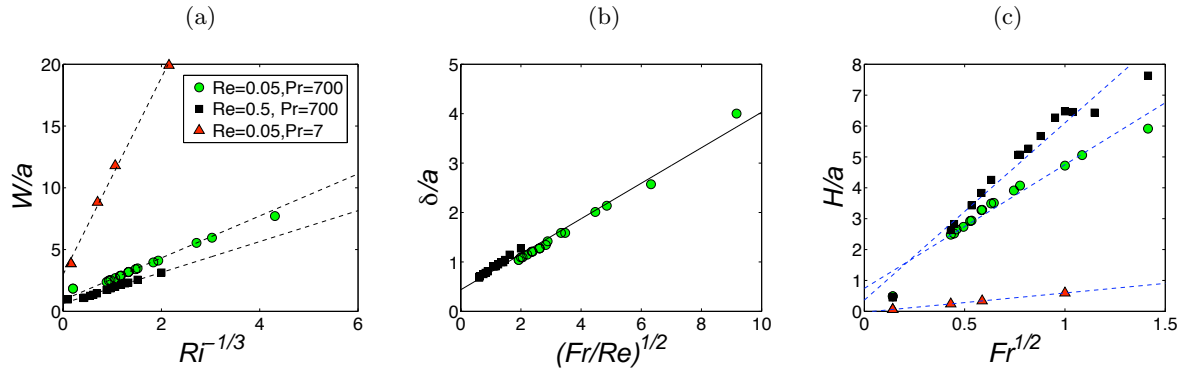


FIGURE 13.

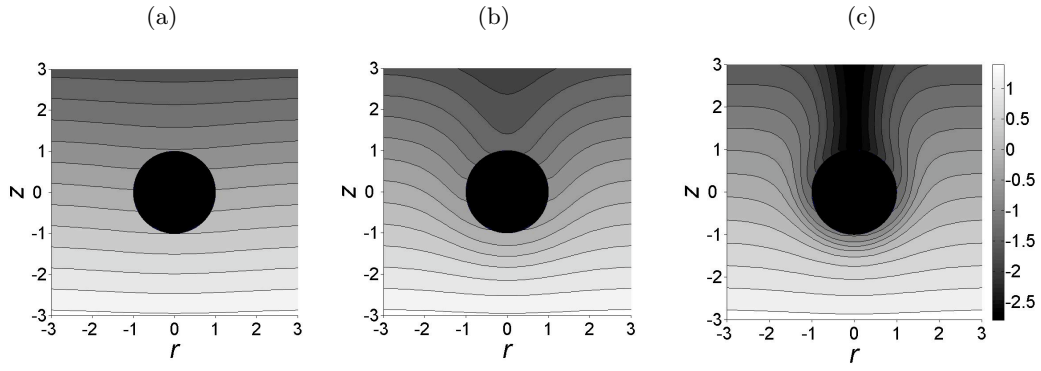


FIGURE 14.

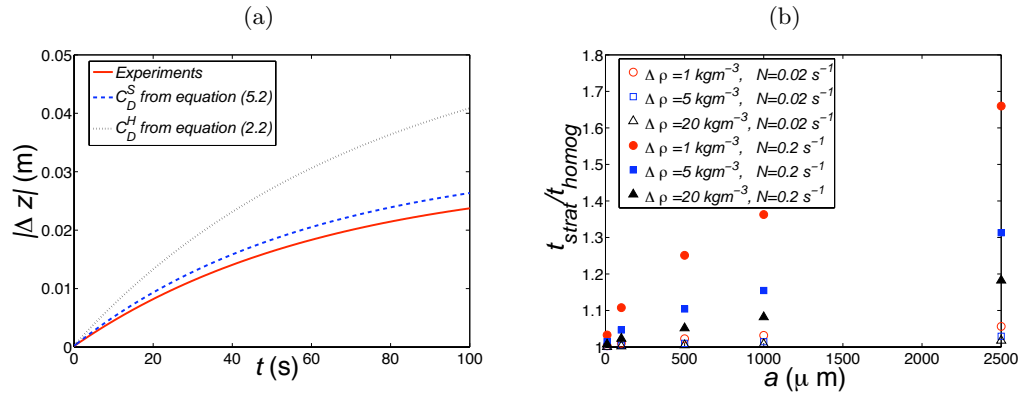


FIGURE 15.